AIAA 93-1043

" Thrust Vector Control Algorithm Design for the **Cassini** Spacecraft

F'. J. Enright

Jet Propulsion Laboratory

Pasadena, Calif.

AIAA/AHS/ASEE

Aerospace Design Conference

February 16-19, 1993 /Irvine, CA

Thrust. Vector Control Algorithm Design for the Cassini Spacecraft

Paul J. Enright*
Jet Propulsion Laboratory, California Institute of Technology
Pasadena, California, 91109

A preliminary design of the Cassini Thrust Vector Control algorithm which controls the spacecraft attitude during main engine burns is described. The discussion includes software architecture, sensor/actuator characteristics, and vehicle dynamics, as well as controller design and margin analysis via classical methods, and performance evaluation via simulation. Special attention Is paid to actuator modeling, propellant dynamics, and to potential controller interactions with structural flexibility and propellant slosh.

Introduction

The Cassini spat.ccraft (Fig. 1) is designed for a four-year orbital tour of the Saturn system, with delivery of the Huygens Probe (ESA) into the atmosphere of Saturn's largest moon, Titan. Cassini is scheduled for an October 1997 launch on a Titan IV with the Centaur upper stage. The mission design includes gravity-assist flybys of Venus, Earth, and Jupiter, and eventual rendezvous with Saturn in June 2004.

The interplanetary cruise trajectory requires a large maneuver between the Venus flybys, and as many as twenty smaller trajectory correction maneuvers (TCMs) for navigation. The orbital phase begins with the long Saturn-orbit insertion burn just after periapse, followed by a periapse raising maneuver at apoapse, which establishes the initial tour orbit. The probe is released on a Titan impact trajectory, and after performing a small deflection maneuver, the orbiter records the probe data as it enters Titan's atmosphere.

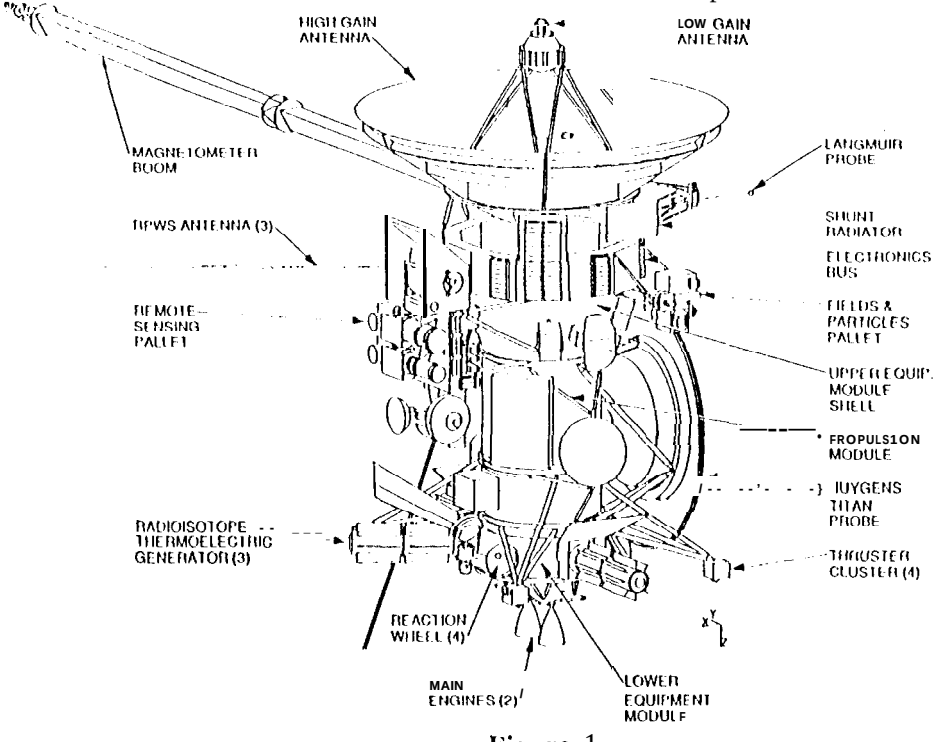

Figure 1
The Cassini Spacecraft

* Member Technical Staff

The orbital tour includes many small TCMs, targeting the orbiter for flybys of Titan and the icy satellites Rhea, Dione, Iapetus, and Enceladus.[1]

Almost all of the required Av is delivered by the (selected) main engine, a 490 N bipropellant thruster, which burns MM]] and N_2O_4. (1'here arc two identical main engines for redundancy.) At launch, the total bipropellant load is 3000 kg, which is 60% of the spacecraft's launch mass. The separate Reaction Control System (RCS) consists of sixteen 0.65 N monopropellant thrusters (eight redundant pairs) fed by a single tank which contains 132 kg of hydraz inc at launch. The RCS is used for cruise attitude control and for momentum management during the orbital phase when the reaction wheels arc in USC. The system can also be used for small Av maneuvers. Each main engine is mounted to the "bottom" of the spacecraft in a gimbal system, allowing two axes of articulation for thrust vector control (TVC) during burns. The third axis (roll about the thrust vector) is controlled using the RCS thrusters.

A variety of propulsive systems have been used for J 1'1, interplanetary orbiters. Recently, the Magellan spacecraft was inserted into Venus orbit using a STAR-48 with 100 lbf hydrazine thrusters for attitude control during the burn. Mars Observer will usc two (of four) fixed 110 lbf biprop engines, attitude control being provided by smaller biprops. Finally, the dual-spin Galileo spacecraft will usc its single 400 N biprop for Jupiter-orbi[insertion, relying on spin stabilization at 10 rpm. The heritage of the current design goes all the way back to Mariner 9, which used a gimbaled 300 lbf engine for insertion into Martian orbit.[2] (The Viking Orbiter design was similar.) For a three-axis stabilized spacecraft, the primary advantage of the gimbaled engine design is that it eliminates the need for intermediate-sized thrusters dedicated to attitude control during the bum The block-redundant Cassini design also provides single-fault tolerance for the engine and its gimbal actuators, which must bc capable of performing as many as 200 bum over the 11-year mission.

This paper describes a preliminary design of the Cassini TVC algorithm. Although the control logic itself is ultimately distilled into a fcw lines of code scattered over several software modules, the analysis of the "algorithm" as a functional unit necessitates the definition of the context in which the controller must perform. The bulk of the work involves modeling of sensors, actuators, and vehicle dynamics, understanding software characteristics, especially timing issues and 1/0 functions, and formulating a concise definition of what the algorithm is supposed to do, and how accurately it needs to do it. (This can be more difficult than it sounds.)

First, the overall software "architecture" is described, at least tbc subset which supports the TVC algorithm. This is followed by a discussion of hardware modeling and vehicle dynamics. After control law design and margin analysis via classical methods, simulation results arc presented and evaluated in the context of the maneuver err or requirements.

TVC Architecture

Fig. 2 is a data flow diagram for the TVC algorithm. The shaded blocks represent software "objects," while the white blocks arc functions in the attitude controller object that comprise the TVC algorithm. Starting from the top left, the attitude commander provides the commanded spacecraft quaternion q^c which aligns the selected main engine with the desired Av at the initial engine articulation. (I"his articulation will have been calculated to point the thrust vector at the center-of-mass.) The commanded rates ω^c arc zero except duri ng the insertion burn where a slow turn is used to minimize finite-burn 1o SSCS. At the bottom left the attitude estimator uscs star tracker and gyro data to propagate the spacecraft attitude with respect to the celestial reference frame. (During burns star tracker data may not be available, in which case the attitude is propagated inertially.) The estimator provides the quaternion, q^e, and the body rates ω^e, which the attitude controller compares to the commanded attitude and rate. The attitude error is decomposed into orthogonal small -angle errors and transformed to a coordinate system which has its 3-axis along the centerl inc of the selected main engine at the initial articulation. Let C be the direction cosine matrix of this fr amc with respect to the spacecraft, so that the transformed position and rate error vectors p and r become:

$$p = 2\,C^T \xi \qquad (1)$$

$$r = C^T (\omega^c - \omega^e) \qquad (2)$$

where ξ is the error rotation vector computed from the error quaternion:

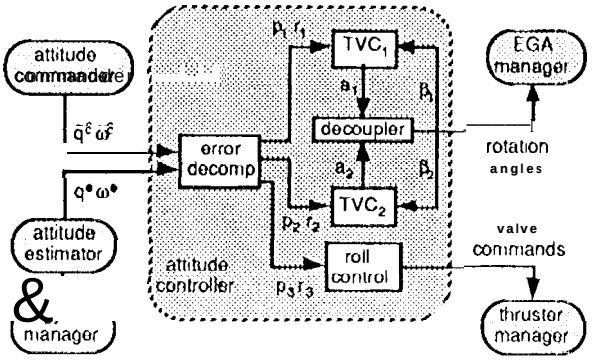

Figure 2
TVC Data Flow

$$\xi_i = \frac{{}^{e}q^{c}_{i}}{{}^{e}q^{c}_{4}} \quad (i = 1,3) \tag{3}$$

with ${}^{e}q^{c} = (q^{e})^{*}\, q^{c}$. (The asterix denotes conjugation, and juxtaposition denotes quaternion multiplication, i.e. successive rotation.)

The 1- and 2- components of the position and rate errors drive two single-axis TVC controllers, which output acceleration requests $a = [a_1 a_2]^T$. (The design of the controller is discussed at length below.) The decoupler transforms these requests into engine rotation commands $\beta = [\beta_1 \beta_2]^T$, using spacecraft mass properties and engine characteristics:

$$\beta = \frac{I^{R} a}{F\, r} \tag{4}$$

where I^R is the upper left 2x2 partition of the inertia matrix transformed into engine coordinates, F is the main engine force, and r is the distance from the main engine to the spacecraft center-of-mass. The rotation commands arc sent to the EGA manager, which computes the necessary extension commands for the linear Engine Gimbal Actuators. These angles are also fed back to the guidance. loops of the TVC controllers (discussed below). The 3-component position and rate errors drive the, roll control logic, which schedules RCS thruster activity with (hc thruster manager.

Sensor/Actuator Models

The strap-down integrating gyro package is mounted to the upper equipment module (Fig.]). Every computational cycle (125 ms) the gyro manager reads the Linlc-tagged angular increments accumulated since the previous read. (One pulse corresponds to 8 μrad.) The attitude estimator propagates the spacecraft quaternion using a second-order expansion of the quaternion kinematic equation, and derives rate using the firsL-order difference. The dynamics of the gyro rebalance loop arc modeled as a damped second-order system with a 5 Hz bandwidth, and an integral pole at 0.5 Hz. White noise inputs in acceleration and rate integrate to rate and position random walks. Although the simulation model includes the pulse-generation logic, the linearized "design model" ignores the quantization altogether, 8 μrad being negligibly small in the TVC environment. The transfer function representation is as follows:

$$H_{gyro}(s) = \frac{Z(s)}{P(s)} = \frac{bs + a}{s^3 + cs^2 + bs + a} \tag{5}$$

with a = 3102. $(rad/s)^3$, b = 1118 $(rad/s)^2$, and c = 89.2 rad/s. (Note that if star tracker data is available during the burn, it will bc used 10 update the inertially-propagated attitude, with a probable one-second update frequency. Closed loop performance with filtered celestial updates has not yet been simulated.)

Figure 3 depicts the Main Engine Assembly (MEA), with the two independently-gimbaled 490 N engines each controlled by two linear Engine Gimbal Actuators (EGA's), An EGA is a ballscrew assembly driven by a brushed DC motor, and each is mounted to the thrust plate via a universal joint. The output shaft is connected by a pin joint to the engine above the gimbal plane, so that extension or retraction of the actuator causes the engine to rotate in its gimbal system.

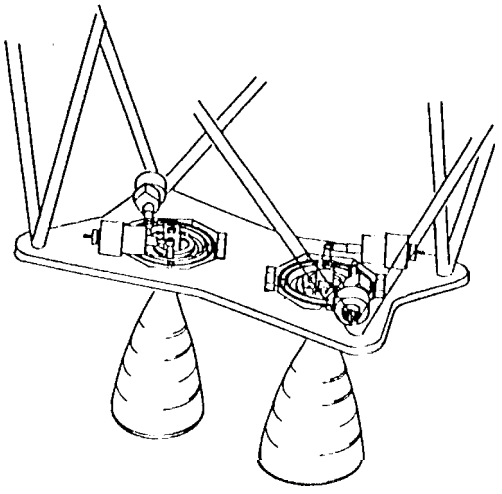

Figure 3
Main Engine Assembly

The exact relationship between actuator extensions ε_1 and ε_2, and the gimbal angles δ_1 and δ_2, is as follows:

$$\varepsilon_i = \sqrt{d_2^2 + 2 d_2 q_i} - d_2 \quad (i = 1,2) \tag{6}$$

with

$$q_1 = \frac{d_1^2}{d_2}(1-\cos\delta_2) + \frac{d_1 d_3}{d_2}\sin\delta_2(1-\cos\delta_1) + d_3\sin\delta_1 + \frac{d3^2}{d_2}(1-\cos\delta_1\cos\delta_2) \tag{7a}$$

$$q_2 = \frac{d_1^2}{d_2}(1-\cos\delta_1) + d_1\sin\delta_1\sin\delta_2 - \frac{d_1 d_3}{d2}\sin\delta_1(1-\cos\delta_2) - d_3\cos\delta_1\sin\delta_2 + \frac{d_3^2}{d_2}(1-\cos\delta_1\cos\delta_2) \tag{7b}$$

where d_1 is the radial offset of the EGA pin joint from the engine centerline, d2 is the actuator null extension, and d_3 is the "lever arm," i.e. the distance from the pin

joint to the gimbal plane. The forward kinematics (6-7) can be approximate.d as follows:

$$\varepsilon_1 \approx d_3\delta_1 + \frac{d_1^2}{2d_2}\delta_2^2 \qquad (8a)$$

$$\varepsilon_2 \approx -d_3\delta_2 + \frac{d_1^2}{2d_2}\delta_1^2 + d_1\delta_1\delta_2 \qquad (8b)$$

Fig. 4 shows the contours of constant engine cone angle from the null orientation mapped to EGA extension space by the exact (solid) and approximate (dashed) forward kinematics. (The ±0.6 inch bounds are the extension limits of the actuators,) Note the significant distortion (from perfect circles) caused by the fairly large radial offset d_1, and also try the attachment of the outer-gimbal actuator to the engine rather than to the gimbal ring.

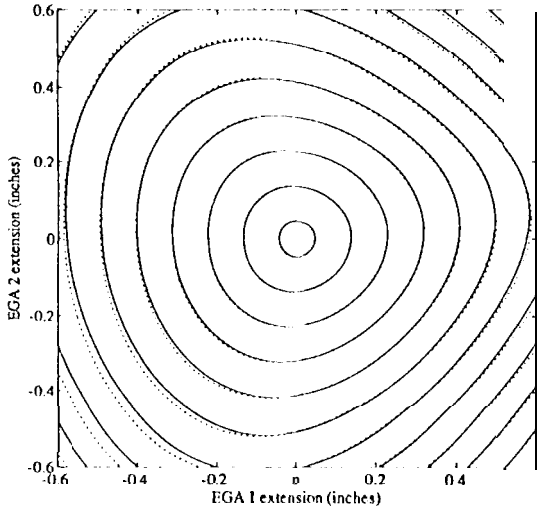

Figure 4
EGA Extensions **for** Constant Cone-Angle Contours of 1°, 3°, 5°, etc.

Every computational cycle, the EGA manager receives engine rotation commands (β) from **TVC,** and converts to gimbal angles. (This involves a twist of approximately 45° for the current MEA **layout.)** The, gimbal angles arc then **converted** to extensions using the **approximate** relations **(8),** and 12 bit extension words arc written to the Engine Gimbal Electronics (EGE). The EGE includes a fast digital loop which controls **actuator** extension using feedback from an LVDT which is **integral** to the **actuator ballscrew.** This is a lc:id-compensated high-gain system with forced saturation, and includes an integral-!ikc term to hold the engine against reflected forces from wind-up of the propellant flex lines. The. motors arc driven by a binary rate modulator (BRM), which converts the 7 bit torque. word into a pulse train. The sample time is 800 μsec, with a minimum BRM pulse-width of 4 μsec, allowing the EGE/EGA servo to bc modeled as a continuous-lime process for TVC. (The simulation model is designed to run with a 5 ms time step for a fourth-order Runge-Kutta integrator, and is not intended to capture dynamics much beyond 20 Hz.)

The actuator dynamics model is essentially a double integrator with a rather elaborate set of enhancements, including back-EMF, viscous fricion, a Dahl model for ball-screw friction, a hysteretic model of the reflected propellant flex line forces, and a model of tile compliance and backlash of the "softmount" which connects the actuator to the thrust plate and provides isolation from launch loads. The actuator dynamics arc integrated separately, with tile output extensions and extension rates being converted to gimbal angles and angular rates for the spacecraft dynamics model, where the engine articulation degrees of freedom arc treated as prescribed motion. This approach captures (hc one-way coupling from the dynamics of the actuator/engine system to the spacecraft dynamics, both through the articulating force vector, and also through inertial torques. (The coupling in the other direction is negligible.) Note that the conversion of extensions (and rates) (o gimbal angle.s (and rates) requires an inversion of the kinematic relationships (6-7) in the simulation software. This is accomplished using a fcw Newton iterations on an initial guess extracted from an approximate inversion of (8).

Fig. 5 shows the response of the system (the EGA Manager, the EGE/EGA servo, and the MEA kinematics) to a 5° step command in the outer gimbal. Tile response is rate-limitc(i, primarily duc to back-EMF. Note the small hang-off duc to the softmount compliance., and also the "cross-axis" response on the other gimbal duc to coupling. This system is fast enough to be almost transparent to the TVC algorithm, which generates command profiles that arc very smooth on this kind of time scale. For the linear

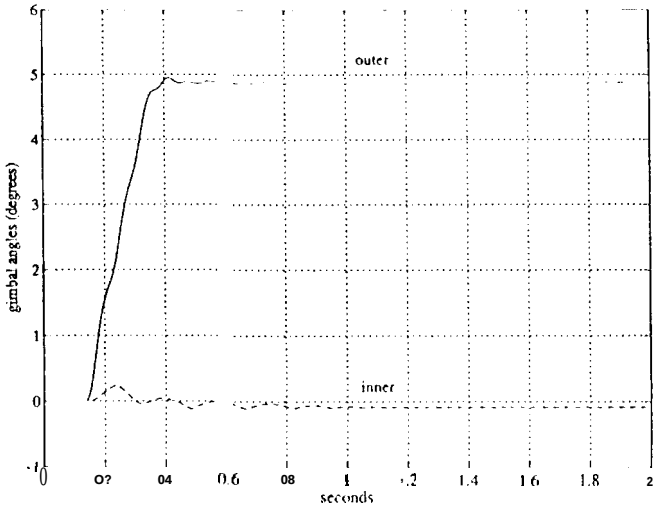

Figure 5
Engine Gimbal Angle Step Response

design model, the system was represented by a first order lag, whose phase shift was matched to the simulated response to a 1Hz sinusoid with an amplitude of 1°). The phase lag, which was taken as the. phase shift of the fundamental Fourier component, was 12.7°, which prompted the following transfer function representation:

$$H_{EGA}(s) = \frac{1}{T_a s + 1} \qquad (8)$$

with $T_a = 0.036s$ (4.4 Hz break).

The thrust profile of the main engine is modeled as an exponential rise to the steady-stm thrust level with a 40 ms rise time.. The RCS thrusters arc modeled similarly with a rise time of 90 ms, and a decay time of ?.50 Ills.

Spacecraft Dynamics

The spacecraft structure is designed around the propulsion module, which houses the two bipropellant tanks (cylindrical with hemispheric heads) in a stacked configuration. Each tank includes a central-sponge type propellant management device (PMD), which exploits surface-tension forces to control the propellant center-of-mass under quiescent conditions. The upper and lower equipment modules attach to the propulsion module (Fig. 1), forming the central structure of the spacecraft, which can be considered rigid in this analysis. Most of the longeron-supported equipment is also very stiff, with resonant frequencies typically 10 Hz and above. Exceptions arc the 1 O-meter magnetometer boom, whose first bending mode lies near 0.7 Hz, and the 3 light RPWS antennas, with bending modes as low as 0.08 Hz.

For the current study, it is adequate to model the spacecraft as a rigid "basebody" with spring-restrained appendages for the mag boom and RPWS antennas. The spring constants arc chosen to match available finite-clcmcnt data. Pendulums arc attached to the base.hotly (along the tank centerlines) to model the propellant slosh under the main engine acceleration. (When the main engine is not on, a different type of propellant model is used, which mimics the "centering" effect of the PMD in the low-g environment.) The pendulum mass, length, and attachment point arc computed using a contractor-supplied program which solves the linearized fluid-dynamic equations using an eigenfunction expansion technique, and derives the mechanical-analogy model parameters for the first lateral mode.[3] Under the main engine. acceleration, the bipropellant pendulums oscillate. near 0.1 Hz. The selected main engine is also modeled as an appendage whose articulation is dictated by the EGA dynamics model discussed above. For simulation, the system equations of motion were generated by a symbolic manipulation code.[4] In future studies, a higher-fidctily model will be used, which incorporates the mag boom and RPWS flexible rnodcs (as well as any other significant flex mode.s) into a central flexible basebody.[5]

For TVC design, the X-axis dynamics can be idealized by the planar system depicted in Fig. 6. Attached to the (shaded) basebody arc the spring-restrained magnetometer boom and two pendulums for the sloshing bipropellant (The RPWS antennas have been truncated on account of their lightness. The RCS monopropellant is discussed below.) The rnag boom bending frequency is almost a decade above the propellant slosh frequencies, insuring that its dynamics can bc considered independentl y. Locking up the propellant degrees of freedom and linearizing the two-body equations of motion results in the following transfer function from engine gimbal angle, y, to the rotation angle of the basebod y, θ:

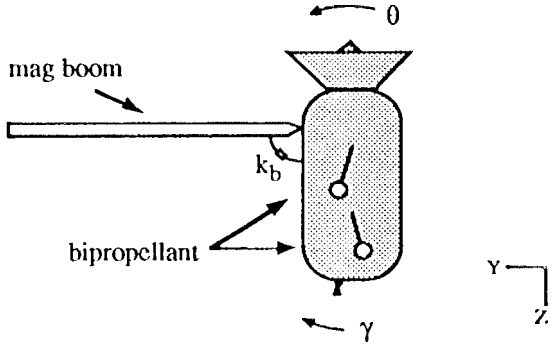

Figure 6
Single-Axis Model with **Mag Boom** and **Bipropellant** Pendulums

$$\frac{\theta(s)}{\gamma(s)} = \frac{Fr}{Is^2} \cdot \frac{\frac{s^2}{\omega_b^2} + 1}{\frac{s^2}{(1+\eta)\omega_b^2} + 1} \qquad (10)$$

where I is the system inertia about its mass center, and $\eta = \frac{R}{1-R}$, with the inertia ratio R defined as:

$$R = \frac{[\, I_b + \mu r_b (r_b + e_b)\,]^2}{I\,(\, I_b + \mu r_b^2\,)} \qquad (11)$$

Here I_b is the inertia of the boom about its own mass center, e_b is the Y separation of the boom hinge from the basebody center of mass, r_b is distance from the boom hinge to the boom center of mass, and the reduced mass $\mu = \frac{m_0 m_b}{m_0 + m_b}$ where m_0 is the basebody mass and m_b is the boom mass. Finally, ω_b is

natural frequency of the appendage with the basebody fixed:

$$\omega_b^2 = \frac{k_b}{I_b + m_b r_b^2} \tag{12}$$

Note that the pole of the transfer function (10) is above the zero (R is small and positive), indicating stable interaction for an "infinite bandwidth" PD (no actuator dynamics). To match finite element data, $(1+\eta)\omega_b$ was set to 0.7 Hz. Viscous damping of 0.25% was added, which is thought to be rather conservative.

The dynamics of the bipropellant pendulums is considered next. Locking up the the mag boom, the linearized three-body equations yield the following transfer function:

$$\frac{\theta(s)}{\gamma(s)} = \frac{Fr}{Is^2} \frac{\left[\frac{s^2}{z_1^2} + 1\right]\left[\frac{s^2}{z_2^2} + 1\right]}{\left[\frac{s^2}{p_1^2} + 1\right]\left[\frac{s^2}{p_2^2} + 1\right]} \tag{13}$$

The zeroes z_1 and z_2, arc given by:

$$\frac{z_1^2}{\omega_p^2} = 1 \tag{14}$$

$$\frac{z_2^2}{\omega_p^2} = 1 + \frac{m_1}{m_0}\left(1 - \frac{b_1}{r_0}\right) + \frac{m_2}{m_0}\left(1 - \frac{b_2}{r_0}\right) \tag{15}$$

where m_0 is the basebody mass, r_0 is the distant.c from the engine gimbal to the basebody center of mass, m_1 and m2 arc the pendulum masses, and b_1 and b2 arc from the base.body center of mass to the pendulum hinges. The normalizing frequency ω_p is tbc usual pendulum frequency under the main engine accelerat ion:

$$\omega_p^2 = \frac{F}{m r_p} \tag{16}$$

where $m = m_0 + m_1 + m2$, and r_p is the pendulum length. (The lengths arc identical duc to the fact that MMH and NTO burn l-to-l volumetrically.) The denominator biquadratic is generally not factorable; however, under the assumption that the pendulum masses m_1 and m_2 arc small with respect to the basebody mass mo, the poles can be approximated as follows:

$$\frac{p_1^2}{\omega_p^2} = 1 + \frac{m_1 b_1 (r_p + b_1)}{I_0} + \frac{m_2 b_2 (r_p + b2)}{I_0} \tag{17}$$

$$\frac{p_2^2}{\omega_p^2} \approx 1 + \frac{m_1}{m_0} + \frac{m_2}{m_0} \tag{18}$$

where I_0 is the inertia of the basebody. For Cassini mass properties and geometry the ordering of the singularities is as follows: $z_1 < p_1 < z_2 < p_2$. As was the case with the spring-restrained appendage, this pattern implies stable infraction with the controller. This is remarkable since the top tank taken in isolation would be unstably interacting due to its "forward" location. (This type of stabilizing phenomenon in multitank situations, and also the approximation leading to (17) and (18) were discussed by Greensite.[6])

In terms of disturbances to tbc basebody, the worst-case propellant fill is in the 50-60% range, where the pendulum masses approach 300 kg (MMH) and 500 kg (NTO). Generating the pendulum models and evaluating (13)-(1 8), it is found that the poles and zeroes arc clustered around 0.1 Hz. Although extremely low damping levels have been observed in "clean" propellant tanks,[7] it is thought that the presence of the PMD will enhance the damping level. Viscous damping of 1% was added to the pendulum models.

Although the RCS tank holds a significant amount of hydrazine, the design include.s an elastomeric diaphragm for buhblc-free expulsion in zero-g. It is expected that the presence of this diaphragm will result in greatly reduced motion, with frequencies and damping levels well above those that would be predicted by a clean-tank pendulum model. As a placeholder, such a pendulum was included in the simulation model. Its frequency is just above the bipropellant slosh modes, although it is much smaller, and it is stably -interacting.

Finally, inertial effects of the articulation of the main engine need to be considered. For a rigid spacecraft, this is known to introduce a pair of imaginary zeroes at the frequency where inertial forces of the articulating engine exactly cancel the thrust-vector moment (usually referred to as the "tail-wags-dog" zero[8,9]). The frequency is given by:

$$\omega_d^2 = \frac{Fr}{I_e + m_e r_{er}} \tag{19}$$

where I_e is the moment of inertia of the engine about the gimbal axis, m_e is the engine mass, and r_e is the distance from the engine center of mass to the gimbal point, The 5 cm engine balancing requirement keeps the TWD zero above 4.4 Hz for current Cassini mass properties.

Control Design and Analysis

Fig. 7 shows the complete linearized X-axis model which was used for TVC design. As depicted the output of the TVC block is a gimbal angle command, which is delayed, held, and passed through the EGA firsl-order lag to result in the engine. gimbal angle. Obviously this is a gross simplification of the. data

flow between TVC and the EGA manager previously depicted in Fig. **2.** Here the gimbal angle is relative to the initial thrust vector orientation, and drives the spacecraft dynamics model after being augmented by [he, "pre-aim" error ε_p, which is the angle between the initial engine thrust vector and the vector from the engine gimbal through the system center of mass. (Due to mass property uncertainties and various misalignments, this can be as large as 1° for the first burn.) The spacecraft dynamics model is a cascade of the transfer functions derived above, evaluated at current mass property estimates for a 50% bipropellant fill. Included arc the lightly damped mag boom bending mode, the coupled bipropellant slosh modes, and the rigid body mode which has been combined with the TWD zero. The output of the double-integrator is the basebody angle, which feeds the 3rd-order gyro model. At this point the sensed angle is sampled and sent to the controller, along with the back-differenced rate estimate. This is a simplification of the process which occurs in the attitude estimator, the, attitude commander, and the error decomposition block of Fig. 2, which is made possible by the single-axis reduction and the restriction to small errors. Note that it has been assumed here that the commanded position and rate arc both zero.

I'here is a clear desire to maintain the controller bandwidth as large as possible, not only to minimize the maneuver errors, but also to keep spacecraft rates to an acceptable level during the transient that follows ignition. ('l'his is a problem particularly for short burns, where even a moderate rate following engine cut-off may be (ii fficult for the low-authority RCS thrusters to cope with.) Sensors and actuators arc flat out to a fcw Hz, and the Nyquist frequency is at 4 Hz, suggesting that the system is equipped to operate in the **0.5** Hz range without difficulty. This is complicated, however, by the presence of the lightly-damped magnetometer boom bending mode near **0.7** Hz. As mentioned above., the zero-pole type mode is benign in the sense that it interacts stably with an infinite-bandwidth PD controller. But for the system at hand, the phase situation starts to degrade rapidly around 1 Hz, with significant losses resulting from sensor/actualor dynamics, the need to dc.rive rate by back-differencing position, and the proximity of the Nyquist. This is exacerbated by the computational delay of 125 ms (an entire sampling period), which at 1 Hz already contributes 45° of phase lag. The desire to accommodate a one-sided requirement on mag boom frequency ($\omega_b > 0.7$ Hz) prompted a gain-stabilization approach for the preliminary design, with a bandwidth of 0.07 Hz. If the boom frequency comes in high, or if damping estimates improve, it would become feasible to design in the 0.1-0.2 Hz vicinity; however, simulation results presented below indicate that even the slower design meets the performance requirements.

As is evident from Fig. 7, the pre-aim error ε_p comes in as a constant disturbance torque, and the system response to this dc.serves some attention. The physics of the problem dictates that the stca(ty-state situation has the thrust vector pointing through the system center of mass, i.e. $\gamma_{ss} = -\varepsilon_p$. The. necessary basebody pointing error to drive this offset would be $\theta_{ss} = \varepsilon_p/k$, where k is the position-to-gimbal gain, and the resulting thrust vector would be rotated by $(1+1/k)\varepsilon_p$ with respect to its initial orientation. This error is unacceptable, and is remedied by positive feedback of the commanded gimbal angle with a gain of 1+k, as shown in Fig. 8, which makes the steady - stale. gain from θ_c to y equal 10-1. Lag is required in the feedback loop to abate its destabilizing effects on the. main loop. This design was adapted from the analog Mariner 9 design,[2] where it was termed "path-guidance," it being viewed as a rather degenerate form of the more general "guidance loop" associated with missile autopilots. Sornc block-diagram algebra reveals that this compensation can be rewritten as a combination of outer-loop gimbal feedback with

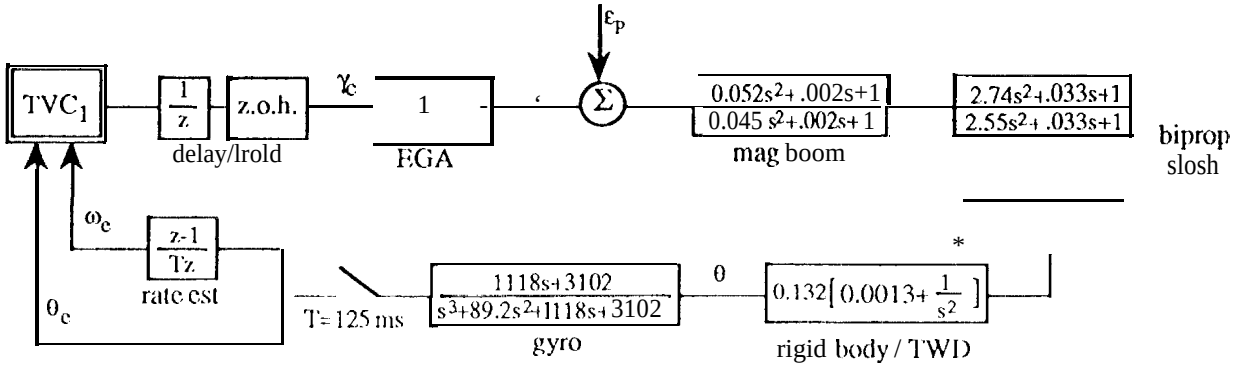

Figure 7
TVC X-axis Block Diagram

integral control in the forward path, similar to the design recently outlined by Wie.[10]

The complete controller with a lead compensation time constant of 6 seconds and a guidance time constant of 10 seconds is shown in Fig. 8. The forward gain (basebody rotation to gimbal angle) is 0.7. The roll-off filter is second order, with poles near 0.3 Hz. The symbol Z{ } denotes a discrete equivalent via bilinear transform with pre-warping.

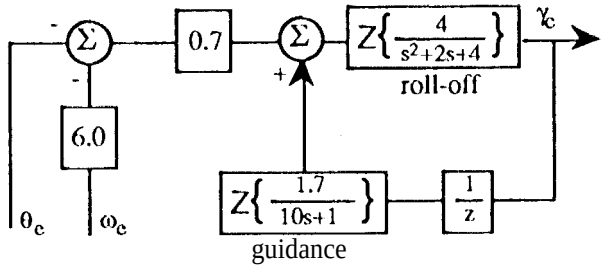

Figure 8
TVC Controller

The open-loop gain-phase plot of the system is shown in Fig. 9. The lower and upper gain margins are -10 dB and +7 dB. The zero-dll crossing is just above **0.07** Hz with 30° of phase margin. The bipropellant nmdcsarcpbasc-stable with frequency-variation margins better than a factor of two in either direction. The mag boom bending mode is gain-stabilized by 9 dB at the assumed lower frequency and damping bounds. The system step response is shown in Fig. 10. The overshoot is just a few percent, but there's a moderate undershoot.

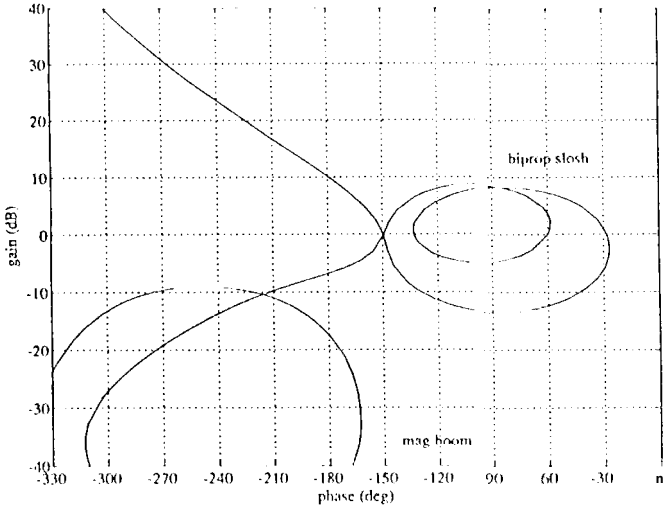

Figure 9
Open-Loop Gain-I'base **Plot**

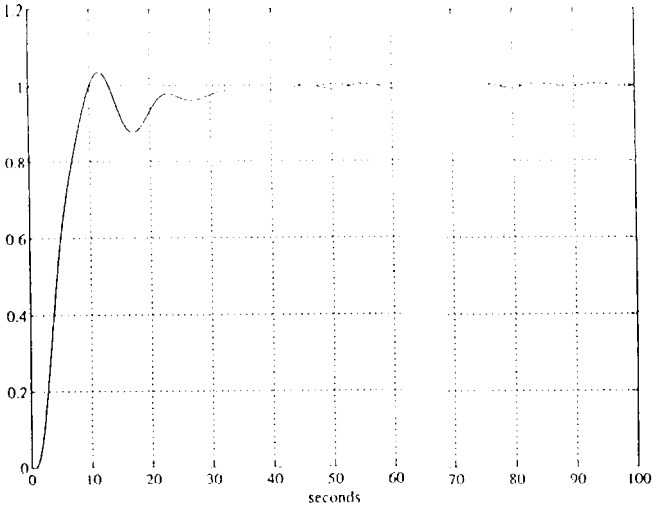

Figure 10
Step Response

The Y-axis dynamics are quite similar to the X-axis dynamics, except for the lack of the mag boom bending mode. (The torsional mode is insignificant.) The TVC_2 block of Fig. 2 was designed by resealing the gains from TVC_1 for the Y-axis inertia, although it can be argued that a higher bandwidth design may be possible for this axis. The roll control logic which drives the RCS thrusters was a simple bang-bang scheme, executing at the 125 ms computational cycle. The rate-to-position gain was 2, and a relatively wide deadzone of $\pm 1^{\circ}$ was used to prevent thruster response to transit.nt disturbances coupling in from the TVC axes, which have little secular content.

Simulation and Performance

The three-axis algorithm performance was evaluated in a simulation environment built around the 12-body spacecraft dynamics model. Included were the full nonlinear models of the gyros, EGAs, and thrusters, supported by preliminary versions of the "hardware manager" software blocks.

Fig. 11 shows the response to a pre-aim error of 10 per axis. The initial attitude error was just 1 mrad per axis, which is a typical deadband for the RCS attitude controller which orients the spacecraft for the maneuver. The bipropellant pendulums were initialized each 30° from the Z-axis, an upper bound which was derived from the requirement that the PMD control the propellant center of mass to 5 cm by the end of a short "quiescent" period immediately prior to main engine ignition.

The first plot of Fig. 11 shows the history of the X-axis orientation angle, which was initialized at 6.2° to align the pre-aim'ed main engine with the Av target at the reference inertial coordinates [0 O -1]. The large disturbance from the sloshing bipropellant is

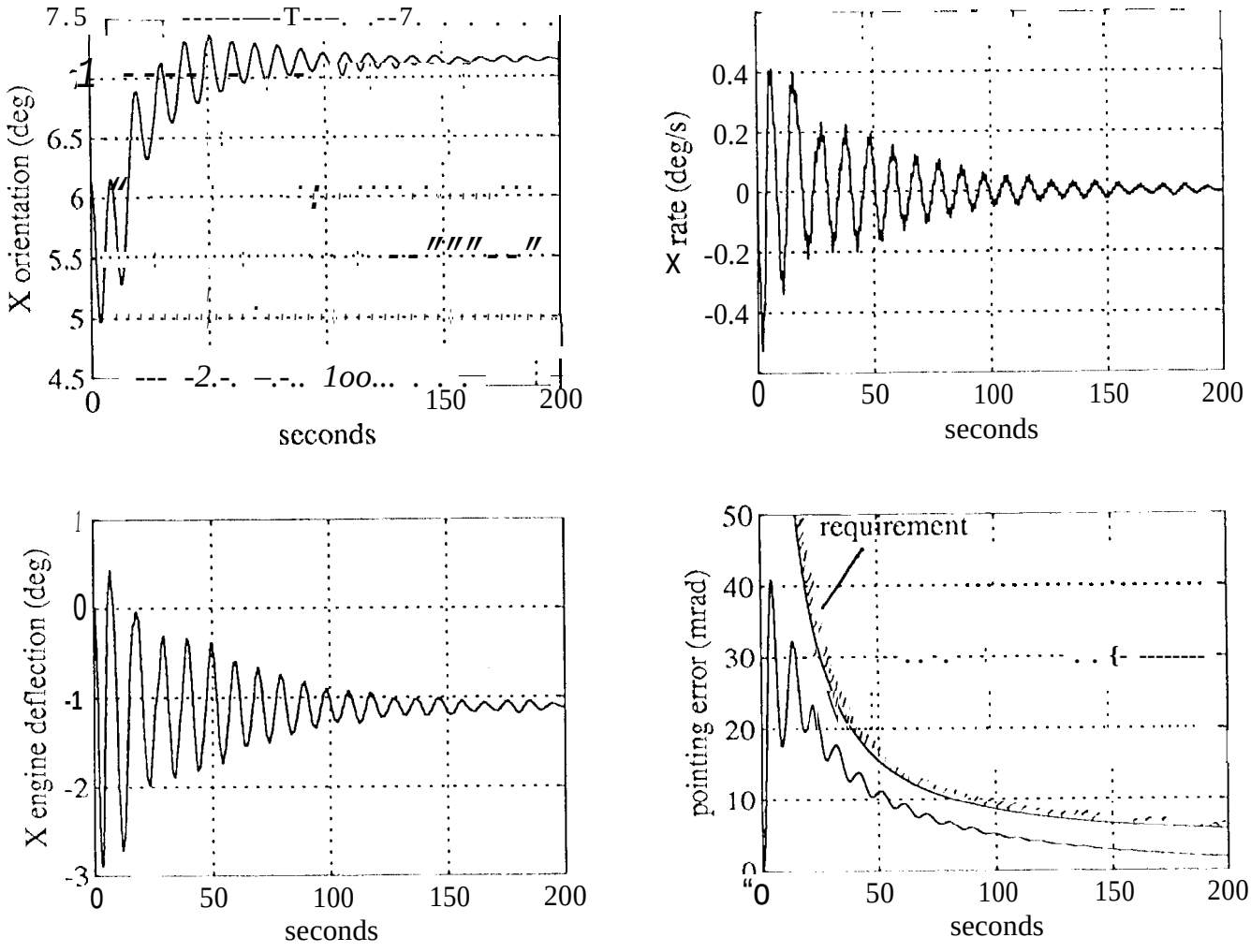

Figure 11
TVC Simulation Results

superposed on the slow guidance loop response, which slews the spacecraft attitude 1° to compensate for the pre-aim error. The second plot shows the spacecraft rate, which peaks out at 0.5 O/s. The mag boom response to the translational acceleration from the main engine is also apparent in this plot. The third plot shows the engine deflection angle, referenced to the pre-aim orientation. The 1° shift points the engine, thrust vector through the equilibrium system mass center. The maximum deflection is 3° from the, initial orientation.

The maneuver Av pointing error is considered 10 bc the sum of 2 distinct contributions. The first of these, referred to as proportional pointing error, is the steady-state misalignment of the thrust vector from the Av target. It is required to be less than 4 mrad. (This is actually a sub-allocation from a maneuver error budget which contains various other contributions, including structural misalignments and attitude determination errors.) The second contribution is referred to as the fixed pointing error, and is defined as the lateral Δv component which results from the transient response due to the pre-aim error. It is required to be less than 100 mm/s. (This is for the uncalibrated case.) These errors arc assumed to be independent, and arc RSSed to form a single requirement on the total Av pointing error, φ, which is defined as the angle between the actual Av vector and the Av target vector:

$$\varphi < \sqrt{(0.004)2 \quad -t \left[\frac{0.1 \text{ m/s}}{\Delta v}\right]^2} \qquad (20)$$

The last plot of Fig. 11 shows the Av pointing error as a function of maneuver termination time, with upper and lower bounds representing the requirement (20). After the first main engine burn, the pm-aim error can bc corrected by analyzing telemetered EGA data. It is clear from Fig. 11 that a burn of at least a minute or so (around 6 m/s) is required, in order to average the data over several cycles of the propellant slosh disturbance. With the recalculated pre-aim, the next main engine burn should have a fixed pointing error well below the calibrated requirement, which is 50 mm/s.

A final note concerning the post-maneuver situation is in order. It is evident from the rate plot in Fig. 11 that short main engine burns can terminate with residual rates as high as 0.5 O/s. The 0.65 N thrusters of the RCS have to fire continuously for 30 seconds to kill this rate, with the spacecraft drifting some 15° from the maneuver orientation. This may aggravate time-line problems for early TCMS, where the time spent near the maneuver attitude. is restricted to minimize the exposure time of certain surfaces to the sun.

Future Work

Further work will focus on controller refinement and optimization as better data become available for the spacecraft structural dynamics, propellant models, and sensor/actuator characteristics. An additional area of interest is the performance during SOI, which has a small rate bias (<1°/min) to minimize gravity loss.

Acknowledgement

This research was carried out by the Jet Propulsion Laboratory, California Institute of Technology, under contract with the National Aeronautics and Space Administration.

References

1. Cassini Project Document 699-116, "Cassini Trajectory Characteristics" (Vol. I and II)
2. Kopf, E.H., "A Mariner Orbiter Autopilot Design," NASA TR 32-1349, Jet Propulsion Laboratory, California Institute of Technology, 15 January 1969
3. Dodge, F.T., and S.T. Green, "Propellant Motion Models for the CRAF/Cassini Spacecraft," Final Report for Project 04-4262, Southwest Research Institute, San Antonio, Texas, March 1992
4. SD/FAST User's Manual, Symbolic Dynamics, Inc., Version B.1.1, July 1991
5. Jain, A., "DARTS - Dynamics Algorithms for Real-'l"imc Simulation of the CRAF/Cassini Spacecraft," JPL D-9308, January 1992
6. Greensite, A.L., "Analysis of Liquid-Propellant Mode Stability of a Multitank Ballistic Booster Vehicle," *Journal of the Aerospace Sciences*, February 1962, pp. 130-139
7. Silverman, S., and H.N. Abramson, "Damping of Liquid Motions and Lateral Sloshing, " Chapter *4* of NASA SP- 106: "The Dynamic Behavior of Liquids in Moving Containers," ed. by H. N. Abramson, 1966
8. Lukens, D. R., A.F. Schmitt, and G.T. Broucek, "Approximate Transfer Functions for Flexible-Booster-and-Aulopilot Analysis," WADD TR-61-93, April 1961
9. Blakelock, J .H., *Automatic Control of Aircraft and Missiles*, John Wiley and Sons, 1965
10. Wie, El., "Thrust Vector Control for a Liquid Upper Stage," *Journal of Guidance, Control, and Dynamics*, Vol.8, No.5, Sept-Oct 1985, pp. 566-572